

Discrete helical modes in imploding and exploding cylindrical, magnetized liners

D. A. Yager-Elorriaga, P. Zhang, A. M. Steiner, N. M. Jordan, P. C. Campbell, Y. Y. Lau,^{a)} and R. M. Gilgenbach

Department of Nuclear Engineering and Radiological Sciences, University of Michigan, Ann Arbor, Michigan 48109-2104, USA

(Received 21 September 2016; accepted 13 November 2016; published online 6 December 2016)

Discrete helical modes have been experimentally observed from implosion to explosion in cylindrical, axially magnetized ultrathin foils ($B_z = 0.2 - 2.0$ T) using visible self-emission and laser shadowgraphy. The striation angle of the helices, ϕ , was found to *increase* during the implosion and *decrease* during the explosion, despite the large azimuthal magnetic field (>40 T). These helical striations are interpreted as discrete, non-axisymmetric eigenmodes that persist from implosion to explosion, obeying the simple relation $\phi = m/kR$, where m , k , and R are the azimuthal mode number, axial wavenumber, and radius, respectively. Experimentally, we found that (a) there is only one, or at the most two, dominant unstable eigenmode, (b) there does not appear to be a sharp threshold on the axial magnetic field for the emergence of the non-axisymmetric helical modes, and (c) higher axial magnetic fields yield higher azimuthal modes. *Published by AIP Publishing.*

[<http://dx.doi.org/10.1063/1.4969082>]

Recently, the magnetized liner inertial fusion (MagLIF)¹⁻⁴ program at Sandia National Laboratories has demonstrated significant fusion neutron yields by imploding a pre-heated, magnetized fusion fuel inside an initially solid cylindrical liner.^{5,6} For these accelerating liners, the dominant instability is the magneto Rayleigh–Taylor instability (MRT),⁷⁻¹¹ possibly coupled to the traditional sausage and kink instabilities.^{12,13} MagLIF liners showed azimuthally correlated structures when no axial field is present,^{14,15} and helically oriented structures when a small external axial magnetic field of 7 T is applied.^{16,17} One mystery is that the helical structures *increased* in pitch angle during the implosion process, despite the extremely large azimuthal magnetic field (>1000 T). An interpretation of this seemingly unusual behavior is given by Weis *et al.* in terms of a discrete, non-axisymmetric eigenmode,¹² entirely analogous to the resolution of the persistence of spiral structures in disk galaxies, despite strong differential rotation.¹⁸ Non-imploding liners have similarly revealed helical structures when an axial magnetic field is applied;¹⁹ no interpretations were given, however.

In this paper, we present magnetized liner implosion experiments and show that when relatively small axial magnetic fields of $B_z = 0.2 - 2.0$ T are applied (compared to the peak azimuthal field, exceeding 40 T), helical striations form in visible self-emission that *increase* in pitch angle as the liner implodes, despite the relatively large azimuthal field outside of the liner, consistent with the helical structures observed by Awe *et al.*^{16,17} We have found that these helical striations persist from the implosion to the explosion stage, when the mean plasma radius increases. We explain these results in terms of a dominant mode of a non-axisymmetric helical instability, whose striation angle is equal to m/kR , where m , k , and R are the azimuthal mode number, axial

wavenumber, and radius, respectively. Using the measured striation angles, we show a dependence of the azimuthal mode number m on the axial magnetic field, with larger axial fields exciting higher m modes, a phenomenon qualitatively explained by our analytic theory.¹²

The instabilities arise from perturbations of the form $\exp(im\theta - i2\pi z/\lambda)$, where m and λ are the azimuthal mode number and axial wavelength, respectively. When $m = 0$, an axisymmetric instability develops. When $m = 1$, a single helical structure arises. Higher m modes result in m intertwined helices. This can be seen by setting the phase of the perturbation to zero, so that $m\theta/2\pi = z/\lambda$; an azimuthal variation of 2π accompanies an axial advance of $m\lambda$. Hereafter, modes with $m \geq 1$ are all designated helical modes, whose helical striation angle is given by $\phi = \text{atan}(m/kR) \sim m/kR$, where $k = 2\pi/\lambda$.

To implode a liner with a sub-megaampere current generator requires an extremely small mass per unit length. Therefore, we used an ultrathin (400 nm-thick) aluminum foil wrapped around a dielectric dumbbell-shaped support structure.²⁰ This thin foil ablates quickly, making its current distribution quite different from MagLIF. However, the onset of kink mode ($m = 1$) is insensitive to the geometry (see, e.g., the $g = 0$ curves in Figs. 2(d) and 2(f) of Ref. 12) so that this thin foil may be used to study the onset of non-axisymmetric modes in an imploding, magnetized liner. The initial foil radius was 3.3 mm, which enabled the liner-plasma to accelerate a distance of over 2 mm before reaching the inner support structure (0.6–1 mm radius, for this experiment). Adjusting the inner radius allows control of the stagnation radius in order to study stagnation and explosion physics.

The experiments were performed on the 1-MA Linear Transformer Driver (LTD) at the University of Michigan.²¹ The experimental configuration and experimental parameters are presented in Fig. 1(a) and Table I. Due to the inductive targets, the peak current was typically 550 kA with 150 ns 10%–90% risetime, and varied as low as 480 kA due to

^{a)}Author to whom correspondence should be addressed. Electronic mail: yylau@umich.edu

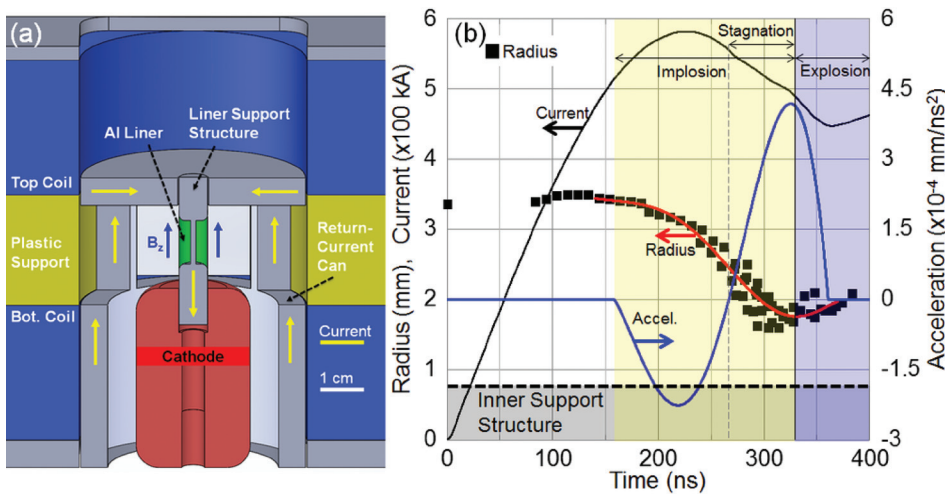


FIG. 1. (a) Experimental configuration. (b) Measured current (s.1172), mean plasma radius, and polynomial fits to radius and acceleration. The mean radius is the average of the distances between all instability bump centers and the z -axis, and characterizes the plasma–vacuum interface.

misfiring in the 40 LTD switches. The axial magnetic field was generated using Helmholtz Coils²² driven by a 5 kV, 1.2 mF capacitor bank. The slow pulse (2 ms base-to-peak) permitted the axial magnetic field to fully diffuse through the load hardware and uniformly pre-magnetize the liner. We employed a novel imaging system combining laser shadowgraphy with visible self-emission.²³ The laser system was formed by trapping a 2 ns, 532 nm freq. doubled Nd:YAG laser pulse within a 3.05 m resonating cavity and sending a small fraction of the beam each trip to backlight the plasma. The backlit image (2 ns shadowgraph) and plasma self-emission (filtered at 532 nm) were of comparable intensities and collected simultaneously using a 12-frame intensified CCD camera (gated at 5–10 ns) to form a series of images over 110 ns, with all images viewed from the same angle of incidence.

The addition of an axial magnetic field resulted in strikingly different instability structures (Fig. 2). The $B_z = 0$ T implosion developed azimuthally correlated self-emission structures that connected the instability bumps and necks on the left and right sides of the plasma (Fig. 2(a)). Even a small axial magnetic field of $B_z = 0.2$ T destroyed this symmetry (Fig. 2(b)). The larger field of $B_z = 0.8$ T appeared to have the smallest amplitude structures, whereas the $B_z = 0.2$ T magnetized liner showed larger structures than the non-magnetized case. This counter-intuitive effect was due to the inner support structure diameter D , which varied for these shots ($B_z = 0.8$ T [s.1168] had the largest $D = 1.5$ mm, whereas $B_z = 0.2$ T [s.1188] had the smallest $D = 1.2$ mm),

TABLE I. Experimental parameters.

| Shot No. | B_z (T) | I_{peak} (kA) | T_{images} (ns) | Characteristic mode $\langle m \rangle$ |
|-------------------|-----------|------------------------|--------------------------|---|
| 1152 ^a | 0 | 550 | 84–184 | ... |
| 1187 | 0 | 480 | 298–368 | -0.1 ± 0.4 |
| 1188 | 0.2 | 550 | 284–384 | 0.3 ± 0.1 |
| 1166 | 0.5 | 530 | 298–348 | 0.9 ± 0.3 |
| 1168 | 0.8 | 550 | 274–314 | 0.9 ± 0.2 |
| 1172 | 1.1 | 580 | 240–290 | 1.8 ± 0.2 |
| 1169 | 1.6 | 570 | 272–292 | 1.4 ± 0.1 |
| 1158 ^b | 2.0 | ... | 308–389 | 1.7 ± 0.2 |

^aStriations not visible during the imaging window.

^bCurrent trace not available.

and due to different peak currents (see Table I). Smaller inner support structure diameters allow the plasma to accelerate and develop instabilities over a longer distance, and larger peak currents result in a larger acceleration and higher MRT growth rate.

To measure the striation angles, a region of interest was chosen near the center of the plasma to minimize curvature effects. For each image pixel across this region, a vertical lineout was taken, where maxima and minima corresponded to bright and dark self-emission striations, respectively. The vertical position of each peak and valley was identified horizontally across the region of interest using a tracking algorithm,²³ and fit using a linear regression. The 3-D striation angle was multiplied by $2/\pi$ to account for cylindrical geometry.¹⁹ Pixels in the images were locally averaged over 10 to 20 pixels to facilitate tracking of bulk features. The images in Fig. 3(a) show the results of this procedure. The two main sources of uncertainty in each measurement were uncertainty in the liner z -axis (estimated at $\pm 1^\circ$, not included in Fig. 3(a)) and uncertainty in fitting the linear regression, which was small. A third source of uncertainty was the standard error for the distribution of the measured striation angles.

For each image, the wavelength was determined by averaging the distance between the centers of all adjacent bumps, and the mean radius was determined by averaging the minimum and maximum radii for an instability bump. The mean plasma radius is plotted in Fig. 1(b) for all shots, excluding shot 1158 (which had the largest support structure) in order to show the distinction between implosion (negative velocity) and explosion (defined here by positive velocity). Figure 1(b) also defines the stagnation boundaries, starting when the acceleration changes sign and ends when explosion begins. The implosion–explosion labels in Fig. 4(a) were individually determined based on the plasma trajectory for a given shot.

To test the hypothesis that the helical structures observed were due to a discrete, non-axisymmetric helical instability, we plotted the average striation angle against the helical pitch angle m/kR for axial fields of $B_z = 1.1, 1.6,$ and 2.0 T, assuming a single helical structure of mode $m = 2$ that is allowed to vary in the radius and the wavelength (see Fig. 4(a)). We found that the mean striation angle was equal to m/kR within

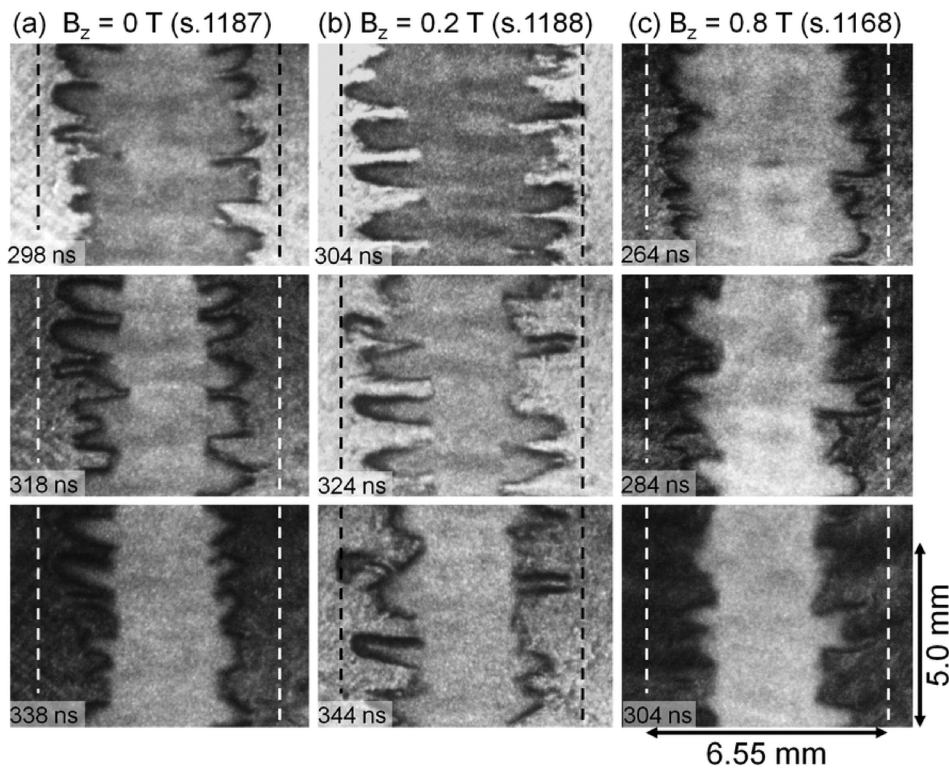


FIG. 2. Series of shadowgraphy/self-emission images for (a) $B_z = 0$ T, (b) $B_z = 0.2$ T, and (c) $B_z = 0.8$ T. For (a) and (b), the top two frames show implosion and the bottom frame shows explosion. For (c), all frames show implosion.

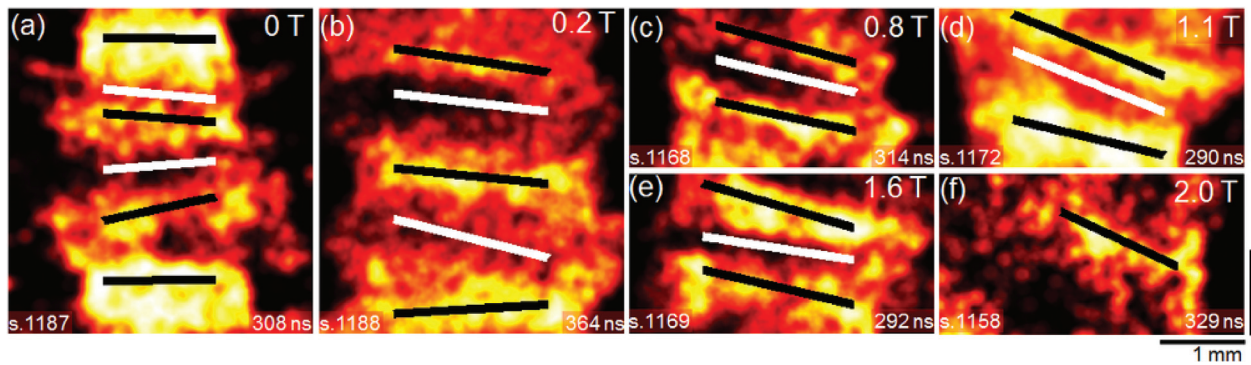


FIG. 3. Self-emission images at 532 nm and measured striation lines. A tracking algorithm,²³ together with a linear fit, is used to identify bright and dark self-emission peaks and valleys, denoted by the black and white lines, respectively. The current is in $-z$, and the axial B field is in $+z$.

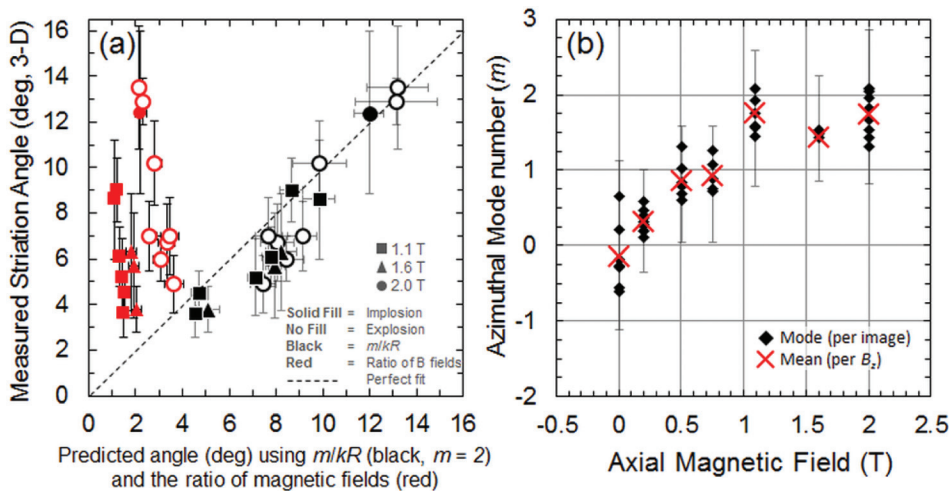


FIG. 4. (a) Plot of measured striation angle against the angle predicted assuming a discrete helical mode with azimuthal mode $m=2$ ($\phi_n = m/kR$, black), and with the predicted angle from the ratio of magnetic fields at time of measurement ($\phi_B = B_z/B_0$, red). The dashed line shows a perfect fit. (b) The azimuthal mode number, determined by normalizing the striation angle to $1/kR$, plotted against the initial axial magnetic field. In (b), the tips of each vertical error bar represent the maximum and minimum values in the corresponding shot.

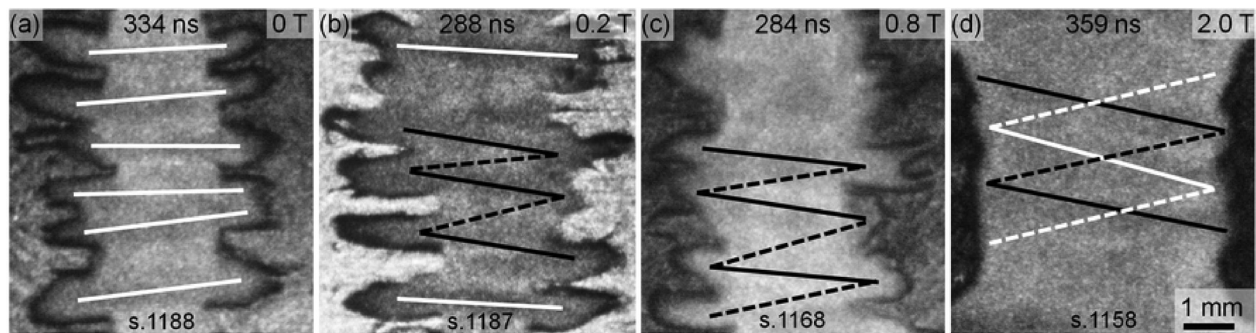


FIG. 5. Shadowgraph images showing the interpretation of characteristic modes from Fig. 4(b). Dark self-emission bands are used to connect the instability bumps on the front (solid lines). Dashed lines connect instability bumps on the back side and are determined by assuming that a similar angle is conserved from the front side.²³ For (a)–(c), the white lines indicate azimuthally symmetric modes and the black lines indicate helically oriented modes. For (d), the black and white lines indicate two intertwined helices, corresponding to the $m = 2$ helical mode.

uncertainty during the evolution of the same shot and for all shots, including both implosion and explosion data. Note that the striation angle increased with decreasing radius during implosion, and decreased with increasing radius during explosion. However, the striation angle could only be correctly predicted when taking into account variation in the axial wavelength (which tended to increase in time) and by assigning²³ an azimuthal mode of $m = 2$. The physical interpretation of two intertwined helices is consistent with the shadowgraphy images (see Fig. 5(d)).

The evolution of the striations could not be explained by the two intuitive notions that: (a) helical features are frozen into magnetic field lines, and (b) helical structures dynamically evolve to maximize the MRT growth, i.e., to minimize magnetic field line bending. Both notions lead to the condition $\mathbf{k} \cdot \mathbf{B} = 0$, i.e., the helix striation angle is given by $\phi_B = B_z/B_\theta$ just outside the plasma at the time of measurement (with B_z assumed fixed at the applied value). The data showed no such trend, with the maximum angle predicted by B_z/B_θ in Fig. 4(a) (in red) being less than 4° , whereas the measured angles ranged from 4° to 14° . Such a deviation is even more evident in Awe *et al.*,^{16,17} where the angle predicted by B_z/B_θ is effectively zero, but the observed helix angle is 16 – 26° .

The fact that the observed helical structures agreed with the predicted pitch angle, despite a dynamically changing radius and axial wavenumber, indicated that there was a dominant helical mode that persisted throughout the discharge. This motivated our systematic study of the dependency of azimuthal mode number on the axial magnetic field. For the unseeded liners used in this experiment, various azimuthal modes ($m = 0, 1, 2$) may co-exist and even merge as the system evolves. For these reasons, we may define a characteristic azimuthal mode number $\langle m \rangle$ as the average of all modes in the plasma for a given shot (and therefore B_z), determined using the following procedure. First, the mean of all modes observed in a single image is found by normalizing the mean striation angle by $1/kR$. For a given shot, the mean mode per image is averaged for all images of that shot to obtain $\langle m \rangle$. These values are plotted in Fig. 4(b) and summarized in Table I as a function of the external axial magnetic field. They are interpreted as follows.

First, Fig. 4(b) shows a small standard deviation in the data about $\langle m \rangle$, meaning that: (a) the characteristic mode persisted throughout the discharge, despite the dynamically changing environment, and (b) there is a dominant m mode, or at most two co-existing m modes. In Fig. 5, we show physical interpretations of the measured characteristic modes for various magnetic fields. Second, even a small axial magnetic field was able to unlock helical modes that are not apparent in the unmagnetized data. The smallest value of $B_z = 0.2$ T was on the threshold for the appearance of helical modes, with both $m = 0$ and $m = 1$ modes co-existing (Fig. 5). As the axial magnetic field was increased to $B_z = 0.5$ and 0.8 T, only the $m = 1$ mode is dominant (Fig. 4(b)). Further increasing the axial field to $B_z = 1.1, 1.6,$ and 2.0 T, generated an $m = 2$ mode that progressively overwhelmed the $m = 1$ mode. Thus, the theory²⁴ that assumes a constant $B_z(t)/B_\theta(t)$ cannot explain Fig. 4(b). Note the two intertwined helices for the $m = 2$ mode, as shown in Fig. 5(d), which was constructed after careful consideration.²³

To explore this dominance, we used the Weis–Zhang theory¹² to study the instantaneous sausage-MRT and helical-MRT growth rates via an ideal MHD, sharp boundary model. The instantaneous radius (and therefore acceleration) was determined by fitting a sixth order polynomial to the mean plasma radii in Fig. 1(b) starting from 140 ns (160 ns for the acceleration). Prior to this start time, the bulk liner motion was small.

Figure 6 shows theoretical growth rates for $B_z = 0, 0.2,$ and 2.0 T using a time-dependent axial wavelength model that approximately matches experimental parameters²⁰ ($\lambda_{80\text{ns}} = 0.3$ mm, $\lambda_{200\text{ns}} = 0.8$ mm, data not shown). Interestingly, for $B_z = 0$ and 0.2 T, the $m = 0$ and $m = 1$ modes have nearly identical growth rates, despite the experiment showing azimuthal symmetry for $B_z = 0$ T and a departure from symmetry for $B_z = 0.2$ T. Increasing the field to $B_z = 2.0$ T showed a dramatic effect on the shape of these growth predictions: the $m = 0, 1,$ and 2 modes are completely stabilized for nearly 100 ns. The $m = 2$ mode becomes the first to destabilize, followed by the $m = 1$ mode, and finally the $m = 0$ mode. This means that there is a window in time when the higher m modes are unstable and can freely grow, whereas smaller m modes cannot. This window exists for any nonzero axial field

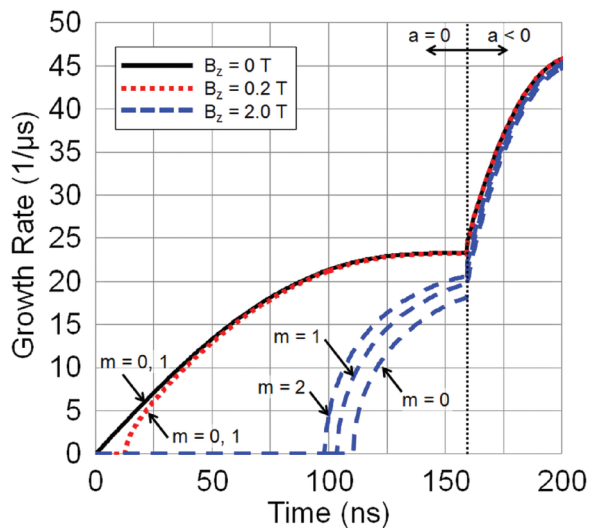


FIG. 6. Growth rate calculations using Weis-Zhang theory for time-dependent experimental parameters (magnetic fields and radius). Estimated parameters were ablated liner-plasma thickness ($500\ \mu\text{m}$) and mass density ($4.5\ \text{kg/m}^3$).²⁰ The wavelength varies according to $\lambda_{\text{mm}} = 0.2 * (\cosh[0.01 * t_{\text{ns}}])$. Liner acceleration begins at 160 ns.

(with stronger effects for increasing B_z); during this time, the general helical shape of the higher m modes may be locked-in (perhaps even modes with $m > 2$). However, if smaller axial wavelength structures merge into larger axial wavelength structures, a common occurrence in RT or MRT, a high m mode may convert into a lower m mode. This last statement follows our way of identifying m from the axial bumps of helical structures, as demonstrated in Figs. 5(b)–5(d). Figure 6 also shows the significant coupling of the classical sausage and helical modes (when there is no radial acceleration) to MRT (when there is radial acceleration¹²). First, there is a dramatic increase in the growth rate, and second, there is a reduction in the disparity between $m=0$, 1, and 2 modes. This indicates that whatever structure has been seeded before this point will persist during the implosion phase; a conclusion consistent with our experimental results, with Awe *et al.*,^{16,17} and with our kink-seeded liner experiments.²³

In summary, our experiments using ultrathin foils demonstrate that (a) there is only 1, or at most 2, dominant azimuthal modes (including $m=0$) for each seeded axial magnetic field, and (b) there is no sharp threshold in the axial magnetic field for the appearance of the helical modes. Gradually increasing the axial magnetic field from zero would simply change the relative importance between the $m=0$ and $m=1$ mode, and (c) the higher axial magnetic field favors higher azimuthal (m) modes. The seeding of these azimuthal modes (including $m=0$) by mechanisms such as electrothermal instability^{25–27} remains an outstanding issue.

Note added in proof: Dr. Edward Ruden kindly informed us that, in his doctoral dissertation (University of California, Irvine, CA, 1988) on gas puff Z-pinch experiments, higher m modes seemed to accompany higher pre-imposed axial magnetic fields.

We thank Dr. Matthew Gomez along with the ABZ group of Sandia National Laboratories for lending us a set of

Helmholtz Coils, utilized in this research. We also thank G. Greening and S. Exelby for experimental assistance. This research was supported by the DOE through award DE-SC0012328, Sandia National Laboratories, and the National Science Foundation. D.Y.E. was supported by an NSF fellowship under Grant No. DGE 1256260. The fast framing camera was supported by a DURIP, AFOSR Grant No. FA9550-15-1-0419.

¹M. E. Cuneo, M. C. Herrmann, D. B. Sinars, S. A. Slutz, W. A. Stygar, R. A. Vesey, A. B. Sefkow, G. A. Rochau, G. A. Chandler, J. E. Bailey, J. L. Porter, R. D. McBride, D. C. Rovang, M. G. Mazarakis, E. P. Yu, D. C. Lamppa, K. J. Peterson, C. Nakhleh, S. B. Hansen, A. J. Lopez, M. E. Savage, C. A. Jennings, M. R. Martin, R. W. Lemke, B. W. Atherton, I. C. Smith, P. K. Rambo, M. Jones, M. R. Lopez, P. J. Christenson, M. A. Sweeney, B. Jones, L. A. McPherson, E. Harding, M. R. Gomez, P. F. Knapp, T. J. Awe, R. J. Leeper, C. L. Ruiz, G. W. Cooper, K. D. Hahn, J. McKenney, A. C. Owen, G. R. McKee, G. T. Leifeste, D. J. Ampleford, E. M. Waisman, A. Harvey-Thompson, R. J. Kaye, M. H. Hess, S. E. Rosenthal, and M. K. Matzen, *IEEE Trans. Plasma Sci.* **40**, 3222 (2012).

²S. A. Slutz, M. C. Herrmann, R. A. Vesey, A. B. Sefkow, D. B. Sinars, D. C. Rovang, K. J. Peterson, and M. E. Cuneo, *Phys. Plasmas* **17**, 056303 (2010).

³S. A. Slutz and R. A. Vesey, *Phys. Rev. Lett.* **108**, 025003 (2012).

⁴A. B. Sefkow, S. A. Slutz, J. M. Koning, M. M. Marinak, K. J. Peterson, D. B. Sinars, and R. A. Vesey, *Phys. Plasmas* **21**, 072711 (2014).

⁵M. R. Gomez, S. A. Slutz, A. B. Sefkow, D. B. Sinars, K. D. Hahn, S. B. Hansen, E. C. Harding, P. F. Knapp, P. F. Schmit, C. A. Jennings, T. J. Awe, M. Geissel, D. C. Rovang, G. A. Chandler, G. W. Cooper, M. E. Cuneo, A. J. Harvey-Thompson, M. C. Herrmann, M. H. Hess, O. Johns, D. C. Lamppa, M. R. Martin, R. D. McBride, K. J. Peterson, J. L. Porter, G. K. Robertson, G. A. Rochau, C. L. Ruiz, M. E. Savage, I. C. Smith, W. A. Stygar, and R. A. Vesey, *Phys. Rev. Lett.* **113**, 155003 (2014).

⁶M. R. Gomez, S. A. Slutz, A. B. Sefkow, K. D. Hahn, S. B. Hansen, P. F. Knapp, and C. A. Jennings, *Phys. Plasmas* **22**, 056306 (2015).

⁷E. G. Harris, *Phys. Fluids* **5**, 1057 (1962).

⁸Y. Y. Lau, J. C. Zier, I. M. Rittersdorf, M. R. Weis, and R. M. Gilgenbach, *Phys. Rev. E* **83**, 066405 (2011).

⁹M. R. Weis, P. Zhang, Y. Y. Lau, I. M. Rittersdorf, J. C. Zier, R. M. Gilgenbach, M. H. Hess, and K. J. Peterson, *Phys. Plasmas* **21**, 122708 (2014).

¹⁰J. C. Zier, R. M. Gilgenbach, D. A. Chalenski, Y. Y. Lau, D. M. French, M. R. Gomez, S. G. Patel, I. M. Rittersdorf, A. M. Steiner, M. Weis, P. Zhang, M. Mazarakis, M. E. Cuneo, and M. Lopez, *Phys. Plasmas* **19**, 032701 (2012).

¹¹T. J. Awe, K. J. Peterson, E. P. Yu, R. D. McBride, D. B. Sinars, M. R. Gomez, C. A. Jennings, M. R. Martin, S. E. Rosenthal, D. G. Schroen, A. B. Sefkow, S. A. Slutz, K. Tomlinson, and R. A. Vesey, *Phys. Rev. Lett.* **116**, 065001 (2016).

¹²M. R. Weis, P. Zhang, Y. Y. Lau, P. F. Schmit, K. J. Peterson, M. Hess, and R. M. Gilgenbach, *Phys. Plasmas* **22**, 032706 (2015).

¹³M. R. Weis, Ph.D. thesis, University of Michigan, Ann Arbor (2015).

¹⁴R. D. McBride, S. A. Slutz, C. A. Jennings, D. B. Sinars, M. E. Cuneo, M. C. Herrmann, R. W. Lemke, M. R. Martin, R. A. Vesey, K. J. Peterson, A. B. Sefkow, C. Nakhleh, B. E. Blue, K. Killebrew, D. Schroen, T. J. Rogers, A. Laspe, M. R. Lopez, I. C. Smith, B. W. Atherton, M. Savage, W. A. Stygar, and J. L. Porter, *Phys. Rev. Lett.* **109**, 135004 (2012).

¹⁵R. D. McBride, M. R. Martin, R. W. Lemke, J. B. Greening, C. A. Jennings, D. C. Rovang, D. B. Sinars, M. E. Cuneo, M. C. Herrmann, S. A. Slutz, C. W. Nakhleh, D. D. Ryutov, J. P. Davis, D. G. Flicker, B. E. Blue, K. Tomlinson, D. Schroen, R. M. Stamm, G. E. Smith, J. K. Moore, T. J. Rogers, G. K. Robertson, R. J. Kamm, I. C. Smith, M. Savage, W. A. Stygar, G. A. Rochau, M. Jones, M. R. Lopez, J. L. Porter, and M. K. Matzen, *Phys. Plasmas* **20**, 056309 (2013).

¹⁶T. J. Awe, C. A. Jennings, R. D. McBride, M. E. Cuneo, D. C. Lamppa, M. R. Martin, D. C. Rovang, D. B. Sinars, S. A. Slutz, A. C. Owen, K. Tomlinson, M. R. Gomez, S. B. Hansen, M. C. Herrmann, M. C. Jones, J. L. McKenney, G. K. Robertson, G. A. Rochau, M. E. Savage, D. G. Schroen, and W. A. Stygar, *Phys. Plasmas* **21**, 056303 (2014).

¹⁷T. J. Awe, R. D. McBride, C. A. Jennings, D. C. Lamppa, M. R. Martin, D. C. Rovang, S. A. Slutz, M. E. Cuneo, A. C. Owen, D. B. Sinars, K.

- Tomlinson, M. R. Gomez, S. B. Hansen, M. C. Herrmann, J. L. McKenney, C. Nakhleh, G. K. Robertson, G. A. Rochau, M. E. Savage, D. G. Schroen, and W. A. Stygar, *Phys. Rev. Lett.* **111**, 235005 (2013).
- ¹⁸F. H. Shu, *The Physical Universe—An Introduction to Astronomy* (University Science Book, Mill valley, CA, 1982), p. 274; G. Bertin, *Dynamics of Galaxies*, 2nd ed. (Cambridge University Press, New York, 2014).
- ¹⁹L. Atoyan, D. A. Hammer, B. R. Kusse, T. Byvank, A. D. Cahill, J. B. Greenly, S. A. Pikuz, and T. A. Shelkovenko, *Phys. Plasmas* **23**, 022708 (2016).
- ²⁰D. A. Yager-Elorriaga, A. M. Steiner, S. G. Patel, N. M. Jordan, Y. Y. Lau, and R. M. Gilgenbach, *Rev. Sci. Instrum.* **86**, 113506 (2015).
- ²¹R. M. Gilgenbach, M. R. Gomez, J. C. Zier, W. W. Tang, D. M. French, Y. Y. Lau, M. G. Mazarakis, M. E. Cuneo, M. D. Johnston, B. V. Oliver, T. A. Mehlhorn, A. A. Kim, and V. A. Sinebryukhov, *AIP Conf. Proc.* **1088**, 259 (2009).
- ²²D. C. Rovang, D. C. Lamppa, M. E. Cuneo, A. C. Owen, J. McKenney, D. W. Johnson, S. Radovich, R. J. Kaye, R. D. McBride, C. S. Alexander, T. J. Awe, S. A. Slutz, A. B. Sefkow, T. A. Haill, P. A. Jones, J. W. Argo, D. G. Dalton, G. K. Robertson, E. M. Waisman, D. B. Sinars, J. Meissner, M. Milhous, D. N. Nguyen, and C. H. Mielke, *Rev. Sci. Instrum.* **85**, 124701 (2014).
- ²³D. A. Yager-Elorriaga, P. Zhang, A. M. Steiner, N. M. Jordan, Y. Y. Lau, and R. M. Gilgenbach, *Phys. Plasmas* **23**, 101205 (2016).
- ²⁴D. D. Ryutov and M. A. Dorf, *Phys. Plasmas* **21**, 112704 (2014).
- ²⁵K. J. Peterson, D. B. Sinars, E. P. Yu, M. C. Herrmann, M. E. Cuneo, S. A. Slutz, I. C. Smith, B. W. Atherton, M. D. Knudson, and C. Nakhleh, *Phys. Plasmas* **19**, 092701 (2012).
- ²⁶K. J. Peterson, E. P. Yu, D. B. Sinars, M. E. Cuneo, S. A. Slutz, J. M. Koning, M. M. Marinak, C. Nakhleh, and M. C. Herrmann, *Phys. Plasmas* **20**, 056305 (2013).
- ²⁷V. I. Oreshkin, *Phys. Plasmas* **15**, 092103 (2008).